Modelling of the Impurity Flow in the Tokamak Scrape-off Layer

J.Neuhauser, W.Schneider,
R.Wunderlich, K.Lackner

IPP 1/216 April 1983

MAX-PLANCK-INSTITUT FÜR PLASMAPHYSIK

8046 GARCHING BEI MÜNCHEN

MAX-PLANCK-INSTITUT FÜR PLASMAPHYSIK

GARCHING BEI MÜNCHEN

Modelling of the Impurity Flow in the Tokamak Scrape-off Layer

J.Neuhauser, W.Schneider,
R.Wunderlich, K.Lackner

IPP 1/216 April 1983

Die nachstehende Arbeit wurde im Rahmen des Vertrages zwischen dem Max-Planck-Institut für Plasmaphysik und der Europäischen Atomgemeinschaft über die Zusammenarbeit auf dem Gebiete der Plasmaphysik durchgeführt.

IPP 1/216

J.Neuhauser, W.Schneider
R.Wunderlich, K.Lackner

Modelling of the Impurity Flow in the Tokamak Scrape-off Layer

Abstract

The impurity flow parallel to the magnetic field lines in a collisional tokamak scrape-off layer is numerically investigated. The rate equations are solved treating each ionization state as a test-fluid, which interacts with the given hydrogen background plasma via collisions and the ambipolar electric field.

Collisional friction usually forces the impurities to flow nearly at hydrogen speed. Thermal forces, however, can become dominant locally for small Mach number and large temperature gradient (e.g. strong divertor recycling), causing in the divertor case impurity accumulation especially near the divertor throat.

In addition self-sputtering at the target plates is calculated, showing the importance of frictional impurity acceleration in addition to the charge state dependent electrostatic energy gain.

1. Introduction and Model

The scrape-off layer in a tokamak or in similar toroidal confinement systems like stellarators is of outstanding importance for the bulk plasma performance as well as for the protection of material walls. Hydrodynamics models have been developed for the behaviour of the hydrogen plasma in this region, where magnetic field lines necessarily intersect material walls. The results show strong inhomogeneity of all plasma parameters (e.g. /1-6/) in reasonable agreement with experiment /7,8/. In this paper we investigate the impurity flow parallel to the magnetic field in a collisional hydrogen scrape-off plasma typical for high density discharges in present tokamaks like ASDEX and for future tokamaks like INTOR. The rate equations are solved treating each ionization state as a dilute testfluid which is coupled to neighbouring states by ionization and recombination and which interacts with the hydrogen background via collisions and the electric field. The background plasma parameters are taken from a hydrodynamic scrape-off model /1,2/.

The testfluid approach requires that the impurity density is low enough, i.e. $\sum_Z Z^2 n_Z \ll n_e \approx n_i$. Here, n_e, n_i and n_Z are the electron and hydrogen density and the density of the Z times charged impurities, respectively. Impurity self-collisions are then ignorable and we may also neglect any feedback from the impurities on the hydrogen background. On the other hand, for the model to be valid, it is required that the collision time between impurities and the background is short compared to the transit time of the impurities over typical spatial dimensions of the problem, e.g. the width of the recycling region. Because of the plasma and source inhomogeneity and the strong dependence of the relevant relaxation times on the charge states a more detailed discussion of the validity of certain results may be necessary in each case. In any case, the present 1D-model is only a first approximation to the at least two-dimensional, fluctuating tokamak boundary and the results should therefore be taken as indicative, only. Alternative approaches to specific impurity problems in the boundary layer can be found e.g. in ref. /9,10/.

2. Equations and Numerical Solution

The impurity ions are described by a set of continuity equations (one for each ionization state) including ionization and recombination from and to neighbouring states:

$$\frac{\partial n_z}{\partial t} + \frac{\partial}{\partial s}(n_z v_z) = S_{z-1} \cdot n_{z-1} - (S_z + R_z) n_z + R_{z+1} n_{z+1} + d_z \qquad (1)$$

($1 \leq z \leq z_{max}$ = atomic number)

s is the spatial coordinate along the field lines, S_z/n_e and R_z/n_e are the ionization and recombination rate coefficients dependent on the electron temperature T_e, and d_z is an externally prescribed source for each individual charge state.

The velocities v_z are determined by the equations of motion for the testfluids, including momentum transfer via ionization and recombination. The coupling to the hydrogen background is described by essential three physically different terms. First, there is an electrostatic force as a consequence of the ambipolar field providing quasineutrality of the background plasma for zero net current and finite electron temperature gradient /11/:

$$n_e \cdot e \cdot E = -\frac{\partial p_e}{\partial s} - 0.71\, n_e \frac{\partial (kT_e)}{\partial s} \qquad (2)$$

(e = electron charge)

$$p_e = n_e k T_e$$

Additional contributions form sources, viscosity etc. /12/ are assumed to be negligible.

The second coupling force is the frictional drag proportional to the velocitiy difference between impurity and hydrogen ions. Here, the electron contribution is usually small. Finally, there are thermal

forces between the background electrons and ions and the impurity ions proportional to the respective temperature gradients. They arise as a consequence of Coulomb collisions in connection with slightly Non-Maxwellian electron and hydrogen velocity distributions caused by finite temperature gradients /13,14,11/. The thermal forces point in the direction of increasing temperature. Of course, a completely analogous force appears between the background hydrogen ions (Z = 1) and the electrons. In order to conserve quasi-neutrality, however, a corresponding electric field is set up (see equ. (2)), which exactly cancels that part of the thermal forces. In contrast, a small number of trace impurities can move freely without remarkable effect on the total electric field or the background plasma parameters. An similar, though much more complicated problem is the impurity transport across the magnetic field in a tokamak /15/.

Keeping only the most important contributions, the equations of motion, including the correct momentum transfer between charge states, are:

$$\rho_z\left(\frac{\partial v_z}{\partial t}+\frac{1}{2}\frac{\partial}{\partial s}v_z^2\right)+\frac{\partial}{\partial s}p_z-n_z\cdot Z e E$$
$$-\rho_z\frac{(v-v_z)}{\tau_z}-\alpha_z n_z\frac{\partial(kT_e)}{\partial s}-\beta_z n_z\frac{\partial(kT_i)}{\partial s} \qquad (3)$$
$$=S_{z-1}\rho_{z-1}v_{z-1}-(S_{z-1}\rho_{z-1}+R_{z+1}\rho_{z+1})v_z+R_{z+1}\rho_{z+1}v_{z+1}-m_z v_z d_z$$
$$\rho_z=n_z m_z\,,\quad p_z=n_z kT_z$$

Here, m_Z is the impurity mass, k is the Boltzmann factor and T_Z is the impurity temperature. Instead of solving an energy equation for each ionization state, we set $T_Z = T_i$ for simplicity. This assumption is slighly inconsistent with the finite relaxation time. But since T_Z enters only in the pressure gradient term, which is frequently small, and in view of other model restrictions this convenient simplification seems to be justified. The coefficients of the collision terms are taken from different references: τ_Z is the slowing down time for small relative velocity, taken from Spitzer /16/, α_Z is

taken according to Braginski /11/ in order to be consistent with the conventions taken for the hydrogen background (see also equ. (2)), while β_Z is taken from Chapman /13/.

$$\tau_z = \frac{3\,(kT_i)^{3/2}\cdot m_z}{4\,(2\pi m)^{1/2}\cdot e^4\cdot Z^2\cdot n_i\cdot \ln\Lambda_i}\,, \qquad n_e = n_i$$

$$\alpha_z = 0.71\cdot Z^2 \tag{4}$$

$$\beta_z = -3\,\frac{1-\mu-5\sqrt{2}\,Z^2\,(1.1\,\mu^{5/2}-0.35\,\mu^{3/2})}{2.6-2\mu+5.4\,\mu^2}\,, \qquad \mu = \frac{m_z}{m_z+m}$$

m is the hydrogen mass and ln Λ_i the Coulomb logarithm.

The total thermal force contribution including the hydrogen-electron term entering via the electric field (equ. (2)) is then consistent with /14/, except for the factor 0.71 instead of 0.8 for the electron contribution. In the appropriate limit the coefficients are also consistent with those used in neoclassical transport theory (Pfirsch-Schlüter regime) /17,18/, except for a 20 percent difference in the asymptotic numerical value of β_Z. In view of the qualitative nature of our model, this specific choice seems to be adequate.

In order to solve this set of equations, we need the following input parameters from the hydrogen background plasma as a function of the coordinate s along the magnetic field lines:

$$n_e\,(s),\ T_e\,(s),\ T_i\,(s),\ v\,(s).$$

In addition we have to prescribe appropriate sources $d_Z(s)$, depending on the physical process, we want to describe. Finally we have the following boundary conditions: At the plasma midplane (s = 0), we have $v_Z = 0$ and $\partial n_Z/\partial s = 0$ because of symmetry. At the target plate (s = L) the ions are neutralized, which means total absorption of ions or equivalently free outstreaming. Therefore, we must not pose a strong boundary condition. Instead, in the numerical code, we set the second derivatives to zero, a weak condition, which allows for sufficient physical freedom.

The numerical solution*) of the time dependent differential equations follows closely the procedure described in /19/. It corresponds to a fast algorithm, in which ionization and recombination are treated alternatively as a perturbation. A non-equidistant numerical grid is used. Because of the weak time dependence of the global plasma parameters in present day tokamaks like ASDEX, we are frequently interested in stationary solutions only. Since, however, the present code as well as the hydrodynamic code providing the background plasma are time dependent, they could be directly coupled in order to describe fast transient phases of the tokamak discharge having time scales comparable to or smaller than the typical scrape-off flow time (e.g. minor disruptions, sawteeth, spiking). For extremly fast processes, however, additional time-dependent terms would arise in the equations of motion /20/. The calculation of the instantaneous radiation losses would be straight forward, too. The rate coefficients used below were compiled by K.Behringer /21/. Charge exchange recombination with hydrogen neutrals has been omitted, since the neutral hydrogen background was not yet calculated in sufficient detail.

3. The hydrogen background plasma

The results presented below are chosen such as to demonstrate the principle features of the impurity behaviour for typical situations occuring in present day and future tokamaks. We adopt the ASDEX divertor geometry sketched in fig. 1 as our main reference case. Typical parameters of the background plasmas as obtained from the hydrodynamic code /1,2/ are shown in fig. 2. They correspond to a total particle and non-radiative energy loss of 10^{22} s^{-1} and 1 MW, resp., from the main plasma, appearing as sources in that part of the scrape-off plasma directly adjacent to the main plasma. The recycling in the divertor chamber, characterized by the pumping time constant τ_N for neutral hydrogen, is assumed to be rather high. Such a situation is typical for most high power discharges in ASDEX /7/ and is expected also for large fusion tokamaks. As can be seen in fig. 2, the flow velocity is subsonic outside the divertor chamber and the total pressure is about constant there. In the divertor chamber, where the recycling occurs, the plasma is gradually accelerated to sound speed. The electron temperature decreases smoothly because of the flattening

*) see: Appendix A

effect of heat conduction. The ion temperature decreases sharply near the divertor entrance, while the density in the divertor is even higher than outside. The electric potential ϕ is positive everywhere ($\sim kT_e$), with a weak maximum inside the divertor, implying a reversal of the electric field $E = -\partial\phi/\partial s$ near the divertor entrance.

With increasing power or decreasing pumping speed ($\sim 1/\tau_N$) the recycling tends to increase and the above features become even more pronounced. A more detailed description and interpretation of the results of the hydrodynamic model is presented elsewhere /2/.

4. Results for typical impurities

Using the parameters of fig. 2, we first present typical charge state and flow velocity distributions for oxygen as a reference impurity for different types of sources. Next the behaviour of helium is discussed because of its principal importance for thermonuclear fusion. Finally, iron is treated as a typical representative for heavier impurities. In addition, iron is well suited to study the details of self-sputtering. Other impurities were also considered (e.g. C, Ne). But since their behaviour can be qualitatively understood on the basis of the above three examples, we omit further details. Results for more restricted physical models (e.g. neglecting intertia or thermal forces) are given in Appendix B.

Oxygen as a reference impurity

First we assume an oxygen source in the main plasma chamber with a Gaussian distribution along the field lines and a decay length of about 4 m (the same as for the hydrogen plasma). Fig 3 shows the results for the assumption that all source particles have charge state OII, e.g. oxygen neutrals released at the wall and immediately ionized in the scrape-off. The charge state distribution plotted in fig. 3a shows a mixture of mainly OIV to OVI near the midplane were the electron temperature is $T_e \approx 40$ eV. Oxygen ions arriving at the target plates are mostly OVI and OV, with a smaller OVII contribution. Of course, this result is a direct consequence of the high

ionization rates up to OVII and the weak recombination rates compared to the residence time of oxygen in the scrape-off ($\sim$ 1 ms).

The total oxygen density exhibits a pronounced maximum just at the divertor entrance. Comparison of the individual forces in equ. (3) shows that in this region the thermal forces become important since especially the ion temperature gradient is large, while the hydrogen flow velocity and therefore the frictional drag is still low. Outside the divertor again the frictional force is dominant. Therefore, near the divertor entrance, the two opposing forces cause impurity accumulation until the resulting pressure gradient is large enough to overcome the retarding thermal force.

The flow velocity (fig. 3b) also shows clearly the retardation at the divertor entrance, while elsewhere the impurities flow at roughly the background velocity, except for the lowest charge states. Because of the Z^2 dependence of the collision frequency, low-Z states first become collision-free rendering a fluid model inapplicable. But in the present case low-Z states are negligible minority anyway.

The strength of the accumulation and the point where it occurs obviously depend on details of the hydrogen recycling in the divertor. If the hydrogen is reionized predominantly closer to the neutralizing target plates, then the impurity peak might occur inside the chamber, where it should be less dangerous. In this sense, the homogeneous recycling source in the divertor chosen for our standard background plasma may be pessimistic.

The density decrease towards the target plates imply results from acceleration of impurity ions and their constant flux (see fig. 3c). The high oxygen velocity at the target plates ($v_Z \approx v$) has important consequences on the sputtering. The kinetic energy of the heavy particles is roughly by the mass ratio higher than the hydrogen energy at sound speed ($m_Z v_Z^2/2 \approx (A/A_H)(kT_e + kT_i)/2$). Together with the electrostatic acceleration in the Debye sheath ($\sim$ 3 ZkT_e) we get for the present example a total impact energy of up to 600 eV and

the iron sputter yield at a stainless steel plate would be around ten percent /22/. Self-sputtering will be discussed lateron.

In reality the oxygen source from the main plasma is a mixture of various charge states. Taking a typical mixture obtained from a one-dimensional solution of the rate equations perpendicular to the magnetic field /19, 2/ we obtain the density distribution along field lines shown in fig. 4. The density mix does not significantly change on the way into the divertor. The reason is that the high charge states, when moving into colder parts, do not have enough time for recombination and low-Z states are a minority anyway. The total oxygen density again shows the same variation as in fig. 3.

The effect of the thermal forces changes significantly when the hydrogen background changes. For example, fig. 5 shows density and velocity profiles along field lines for essentially the same case as in fig. 3, but for lower and higher input power. For 0.3 MW the divertor recycling is lower, the Mach number in the main chamber approaches $M \approx 0.5$. In this case thermal forces become unimportant everywhere and the local density is essentially inversely proprotional to the background velocity (fig. 5a). Such a high Mach number, low recycling scrape-off, however, may be more typical for present day limiter experiments than for a divertor experiment like ASDEX.

For 2 MW, on the other hand, the recycling is even higher, the Mach number falls below $M \approx 0.1$, and the temperature gradients are again steep. Therefore, extremly strong impurity accumulation occurs just outside the divertor (fig. 5c). The local flow velocity is nearly zero. Of course, diffusion across magnetic field lines and a different hydrogen recycling profile could significantly affect the location and amplitude of the peak.

An order of magnitude comparison between the frictional drag and the the thermal forces shows that accumulation occurs when the local Mach number is smaller han the ratio of the hydrogen mean free path, λ_i, to the temperature gradient length, λ_T, i.e. $M \lesssim \lambda_i/\lambda_T$ consistent

with the numerical results. Therefore thermal forces may influence the impurity pumping efficiency in the high recycling regime of future tokamaks.

As a final case a homogeneous OII source in the divertor chamber is considered. For low input power the impurities are quickly accelerated and swept towards the divertor plates with nearly sound speed. The density and the flux increase monotonically towards the plate (fig. 6a). The total oxygen density outside the divertor is several orders of magnitude lower and within the numerical error. Obviously, the impurities are well confined in the divertor chamber by the frictional force. In practice the achievable confiment or "compression" of impurities will be limited by bypasses, allowing for a backflow of neutral impurities into the main chamber. This cannot be discribed correctly within the one-dimensional model.

A quite different behaviour is obtained for the high recycling case (2 MW) as shown in fig. 6b. As in fig. 5c, a density peak forms in front of the divertor and again, in a real geometry, cross diffusion at that point may efficiently remove impurities and deteriorate the impurity retention in the divertor.

Helium pumping

A quantitative assessment of helium pumping would require much more geometrical details and atomic physics than contained in our present model. Nevertheless, a few non-trivial statements can be obtained. For this purpose, we choose a background plasma with high power throughput (2 MW) and strong recycling (midplane: T_e = 48 eV, T_i = 45 eV, n_e = 3 x 10^{19} m^{-3}; target plate: T_e = 14 eV, T_i = 9 eV, n_e = 6 x 10^{19} m^{-3}). Otherwise the profiles are similar to those in fig. 2.

Helium III ions leave the main plasma and flow towards the divertor. In the divertor we prescribe a recycling of 98 percent in from of a homogeneous helium II source, i.e. only weak neutral helium pumping. The high recycling produces a high stationary helium ion pressure in the divertor (fig. 7). This high pressure, however, extends quite a distance

beyond the divertor entrance, again due to the flux retardation by the thermal forces. There is even a small net outflux of helium II towards the main plasma which is ionized and returned as helium III. The thermal force effect, however, is weaker than for oxygen because of the low Z, and disappears for low power throughput and low recycling. On the other hand,it is the high recycling scrape-off which is presently favoured for future tokamaks. We therefore conclude that thermal forces must be considered in any study concerning impurity or ash removal.

Iron Including Self-Sputtering

Iron is treated finally as a typical medium-Z first wall material. Calculations with various source distributions give results quite similar to those for oxygen exept that on the average slightly higher ionization states are reached and thermal force effects are therefore more pronounced. Here we concentrate on self-sputtering at a stainless steel divertor plate.

In order to obtain correctly the total yield we calculate the iron self-sputtering separately for each charge state from the sputtering coefficient $Y(\varepsilon_Z)$, where

$$\varepsilon_z = \frac{m_z}{2} v_z^2 + 3 \cdot Z \cdot k T_e + c\, k T_z$$

The effect of the thermal ion velocity spread around the mean velocity cannot be calculated without a detailed knowledge of the angular dependence of Y and the angle of incidence of the iron ions. But the contribution to the average energy ε_Z is small anyway and setting $c \gtrsim 1$ may be a reasonable approximation.

Self-sputtering results for nickel are used /23/ since more accurate data are available and the difference to iron should be small. The total neutral iron source at the target plate is

$$\Gamma_t = \sum_z \left(n_z v_z \cdot Y(\varepsilon_z) \right)$$

where $n_Z v_Z$ and ε_Z are taken at the plate.

These iron neutrals penetrate the scrape-off plasma at best a few millimeters before they are ionized. In the model, we introduce these ions as a Fe II source, decaying exponentially away from the target plate. The decay length λ_o with respect to the direction of the magnetic field depends on the angle of incidence of the field lines (usually a few degree) and the effective ionization length. It is treated as a free parameter in the following.

The total iron flux enhancement is $\eta = \Gamma_t/\Gamma_p$, where Γ_p is the iron flux originating from the main chamber. An average sputtering coefficient $\bar{Y}$ may then be defined as $\bar{Y} = 1 - \eta^{-1}$.

Fig. 8 shows iron profiles for a low power background plasma (0.3 MW). Though the electron and ion temperature at the wall are only 12 eV and 6.5 eV, the flux amplification is $\eta \approx 3.2$. The main contribution comes from primary particles with a charge state around Fe VI and about hydrogen velocity. The secondary particles, however, are ionized only up to Fe IV in this specific case and then quickly swept onto the plate (Z^2 dependence of the cross section). Their final velocity is appreaciably below the hydrogen speed and for Fe II and probably also Fe III the fluid model may be questionable, though the predicted behaviour will be qualitatively correct.

$\bar{Y}$ has been calculated for various cases by changing the background plasma parameters and the iron penetration depth. As an example, fig. 9 shows $\bar{Y}$ as function of the electron temperature at the target plate and for different source width λ_o of secondary particles. The temperature variation was obtained by changing the power input. A self-sputtering avalanche is obtained for $T_e \approx 20$ eV, depending moderately on λ_o. For comparison $\bar{Y}$ is given for an average $Z = 4$, keeping only the electrostatic acceleration in the Debye sheath, i.e. $\varepsilon_Z \approx 12\ kT_e$. This procedure, which is frequently used as an estimate, generally yields too low sputtering and too high a threshold.

The scaling of $\bar{Y}$ as obtained from the multifluid model may be understood from a simple consideration. If Y_1 is the average sputtering coefficient of primary ions and Y_2 that of secondary ions (usually

$Y_2 < Y_1$), then the sum over infinitely many generations yields a flux amplification

$$\eta = 1 + \frac{Y_1}{1 - Y_2}$$

Obviously, a self-sputtering avalanche is obtained only when $Y_2 \rightarrow 1$, even if Y_1 is large.

In a limiter configuration, a fraction $(1 - r)$ of the secondary iron neutrals may directly enter the closed line region and return as primary ions with sputtering coefficient Y_1. The flux amplification then is

$$\eta = 1 + \frac{Y_1}{1 - r Y_2 - (1-r) Y_1}$$

and the self-sputtering avalanche is obtained when the denominator, now dependent also on Y_1, approaches zero.

5. Summary

The impurity transport parallel to the magnetic field lines in the scrape-off layer of a tokamak has been investigated numerically on the basis of a multifluid model and in the limit of small impurity concentration ($n_Z Z^2 \ll n_e \approx n_i$). The model is a reasonable approximation for high density discharges in present experiments like ASDEX and for the high recycling regime of future fusion tokamaks like INTOR.

Typical impurities occuring in a tokamak (e.g. O, Fe, C, He) have been treated. The behaviour of others may be qualitatively inferred from these results, keeping in mind the different electronic shell structures. In general, the ionization rate is large for low Z states, while recombination is a small effect on the millisecond life time of the impurities in the boundary layer (charge exchange recombination with hydrogen not yet included).

The charge state distribution in the scrape-off is therefore mainly determined by the source distribution. Neutral impurities from ma-

terial walls are quickly ionized a few times, while high Z impurities from the central plasma essentially keep their charge state. The charge state mixture arriving at the target plates therefore has in most cases no similarity with that obtained from local Coronal equilibrium.

For high local Mach number the friction between impurities and the background hydrogen ions is the dominant effect, forcing the impurities to flow at nearly the hydrogen velocity. Efficient impurity removal from the main chamber is obtained. In case of strong impurity recycling in the divertor (e.g. rare gases) impurity "compression" by the frictional drag occurs. Another important consequence is that impurities arriving at the target plates, where the background plasma reaches sound speed, have gained high kinetic energy proportional to their mass. For heavy impurities its contribution to the total impact energy may be comparable or even larger than the electrostatic acceleration in the Debye layer ($\sim 3\ ZkT_e$) with obvious consequences for the target erosion.

For high target recycling the Mach number outside the recycling region becomes quite low and other forces can compete with friction, causing a remarkable slip between impurities and the background plasma. The most significant change occurs just in front of the recycling zone, i.e. near the divertor entrance, where especially the ion temperature drops quickly. Here, thermal forces directed towards high temperature may slow down or even reverse the impurity flow if $M \lesssim \lambda_i/\lambda_T$. Rather pronounced impurity accumulation is found in this region, deteriorating impurity pumping from the main chamber and impurity retention in the divertor. A more quantitative assessment will, however, require a more sophisticated, two-dimensional description of that regime.

Self-sputtering at the target plates has been investigated for iron as a typical wall material. Typically two classes of ions

are obtained. Those originating from the main plasma show a broad mixture of charge states and their self-sputter yield is frequently above one. Secondary iron particles sputtered at the plate are ionized a few times and quickly swept back onto the target. A self-sputtering avalanche is obtained only when the average sputtering yield of these secondary particles approaches one, the threshold temperature being dependent on many parameters.

Acknowledgements:
We thank Dr. K. Behringer for providing his rate coefficient data sets.

References:

/1/ W.Schneider, K.Lackner; International Conference on Plasma Physics, Göteborg, Sweden, 9 - 15 June 1982, paper 11b:3, p. 46

/2/ R.Chodura, K.Lackner, J.Neuhauser, W.Schneider, R.Wunderlich; 9th International Conference on Plasma Physics and Controlled Nuclear Fusion Research, Baltimore, USA, 1982; paper IAEA-CN-41/D-3-1 (Vol. I, p. 313)

/3/ M.Petravic, D.Heifetz, D.Post, W.Langer, C.Singer; ibid; paper IAEA-CN-41/D-3-2 (Vol. I, p. 323)

/4/ J.G.Morgan, P.J.Harbour; Fusion Technology 1980, Vol. 2, p. 1187; Pergamon Press 1981 (Proceeding of the 11th SOFT, Oxford, UK, 1980)

/5/ M.F.A.Harrison, P.J.Harbour, E.S.Hoston; Report CLM-P668, Culham, 1982 (to be published in Nucl. Technology/Fusion)

/6/ M.A.Mahdavi, J.C.DeBoo, C.L.Hsieh, N.Ohyabu, R.D.Stambough, J.C.Wesley; Phys. Rev. Lett. 47, 1602 (1981)

/7/ M.Keilhacker et al.; 9th International Conference on Plasma Physics and Controlled Nuclear Fusion Research, Baltimore, USA, 1982; paper IAEA-CN-41/R-2

/8/ Y.Shimomura, M.Keilhacker, K.Lackner, H.Murmann; to be published in Nuclear Fusion

/9/ H.A.Claassen, H.Repp; Nuclear Fusion 21, 589 (1980)

/10/ S.Sengoku, H.Ohtsuka; J. Nucl. Mat. 93&94, 75 (1980)

/11/ S.I.Braginski; Reviews of Plasma Physics, Vol. 1, p. 205; M.A.Leontovich (Editor); Consultants Bureau, New York, 1965

/12/ P.J.Harbour; Report CLM-RR/E4/3 Culham, UK, 1982 (and private communication)

/13/ S.Chapmann; Proc. Phys. Soc. 72, 353 (1958)

/14/ J.M.Burgers; Symposium of Plasma Dynamics; F.H.Clauser (Editor), Pergamon Press, 1960; p. 119 (see chapter 5 - 17)

/15/ S.P.Hirshman, D.J.Sigmar; Nucl. Fusion 21, 1079 (1981)

/16/ L.Spitzer, jr.; Physics of Fully Ionized Gases, 2nd Edition; Interscience Publishers, New York, 1962

/17/ P.H.Rutherford; Phys. Fluids 17, 1782 (1974)

/18/ V.M.Zhdanov, P.N.Yushmanov; Sov. J. Plasma Phys. 3, 662, 1977 (Fiz. Plazmy 3, 1193 (1977))

/19/ K.Lackner, K.Behringer, W.Engelhardt, R.Wunderlich; Z. f. Naturforschung 37a, 931 (1982)

/20/ A.B.Hassam; Phys. Fluids 23, 38 (1980)

/21/ K.Behringer, private communication

/22/ E.Hechtl, J.Bohdansky, J.Roth; J. Nucl. Mat. 103&104, 333 (1981)

/23/ E.Hechtl, H.L.Bay, J.Bohdansky; Appl. Phys. 16, 147 (1978)

Figure Captions:

Fig. 1: Schematic cross section of the ASDEX divertor tokamak. The shaded scrape-off region between the midplane (s = 0) and the divertor plate (s = L) is treated by a 1D-model as indicated at bottom.

Fig. 2: Variation of scrape-off plasma parameters along magnetic field lines for an ASDEX-type configuration with additional heating and fairly high divertor recycling. s = 0 and s = 15 m correspond to the torus midplane and the divertor plate, respectively. The divertor throat, defined by the edge of the divertor recycling region, is located at s $\approx$ 12 m.

Fig. 3: Normalized densities, velocities and fluxes for oxygen charge states obtained for the background plasma shown in fig. 2. An OII source centred at the midplane (s = 0) is assumed.

Fig. 4: Normalized oxygen charge state distribution for a realistic charge state mixture (maximum at OVII) compared to a pure OII source as in fig. 3.

Fig. 5: Normalized oxygen charge state distribution and velocity for different power through-put and hence different divertor recycling and Mach number outside the divertor (OII source at midplane).

Fig. 6: Normalized oxygen charge state distribution for different power through-put. In contrast to fig. 5 a homogeneous OII source in the divertor chamber is assumed.

Fig. 7: Helium II and III distribution along field lines. A He III source at the midplane and a He II recycling source in the divertor are assumed (98 % recycling).

Fig. 8: Normalized densities, velocities and fluxes of iron ionization states for low power through-put including self-sputtering at the target plates.

Fig. 9: Effective iron self-sputtering yield as function of the electron temperature at the target plate. The neutral iron penetration length is parameter. The dashed line represents an estimate based on an average Z and electrostatic sheath acceleration only.

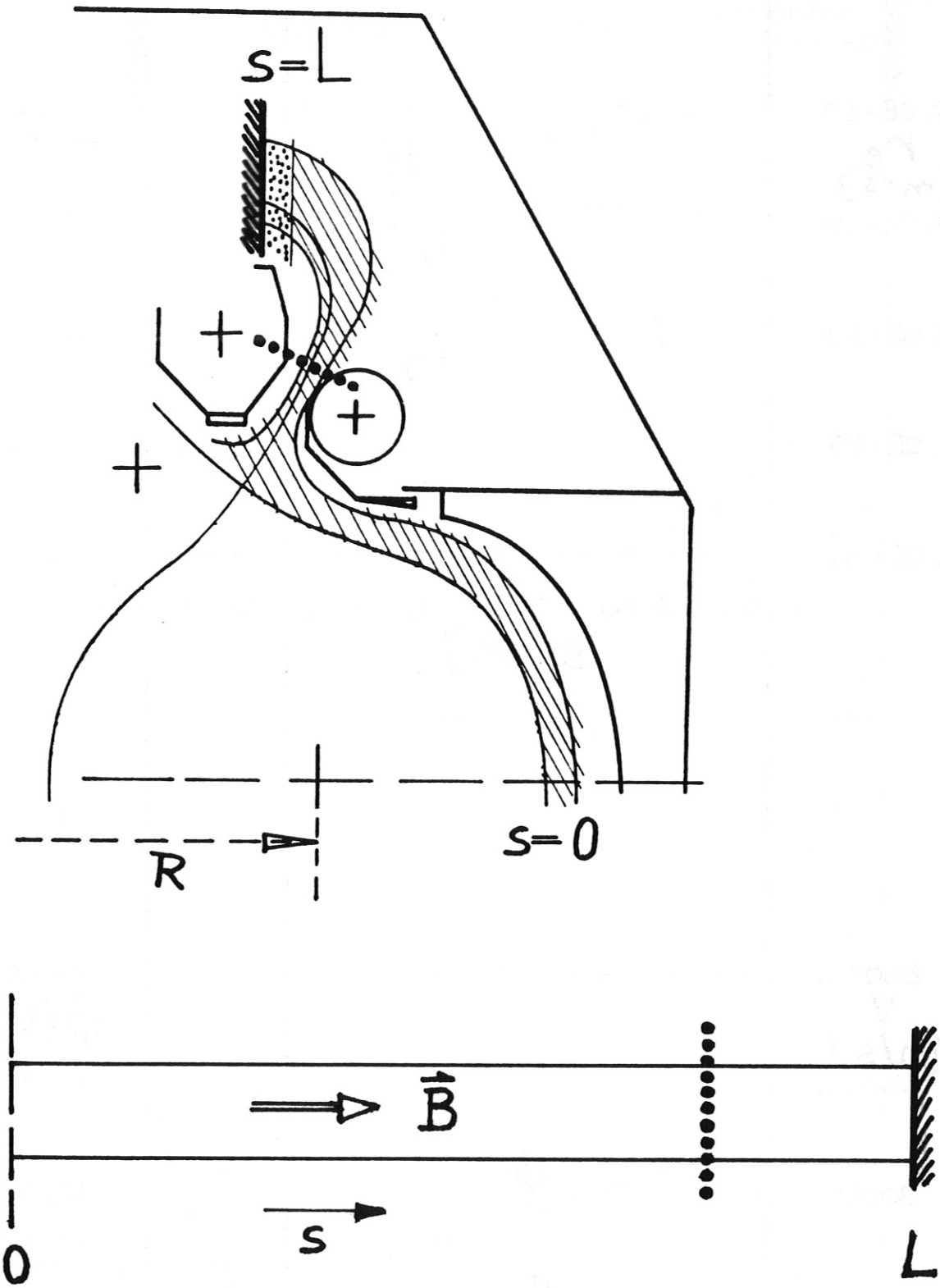

Fig. 1

Fig. 2

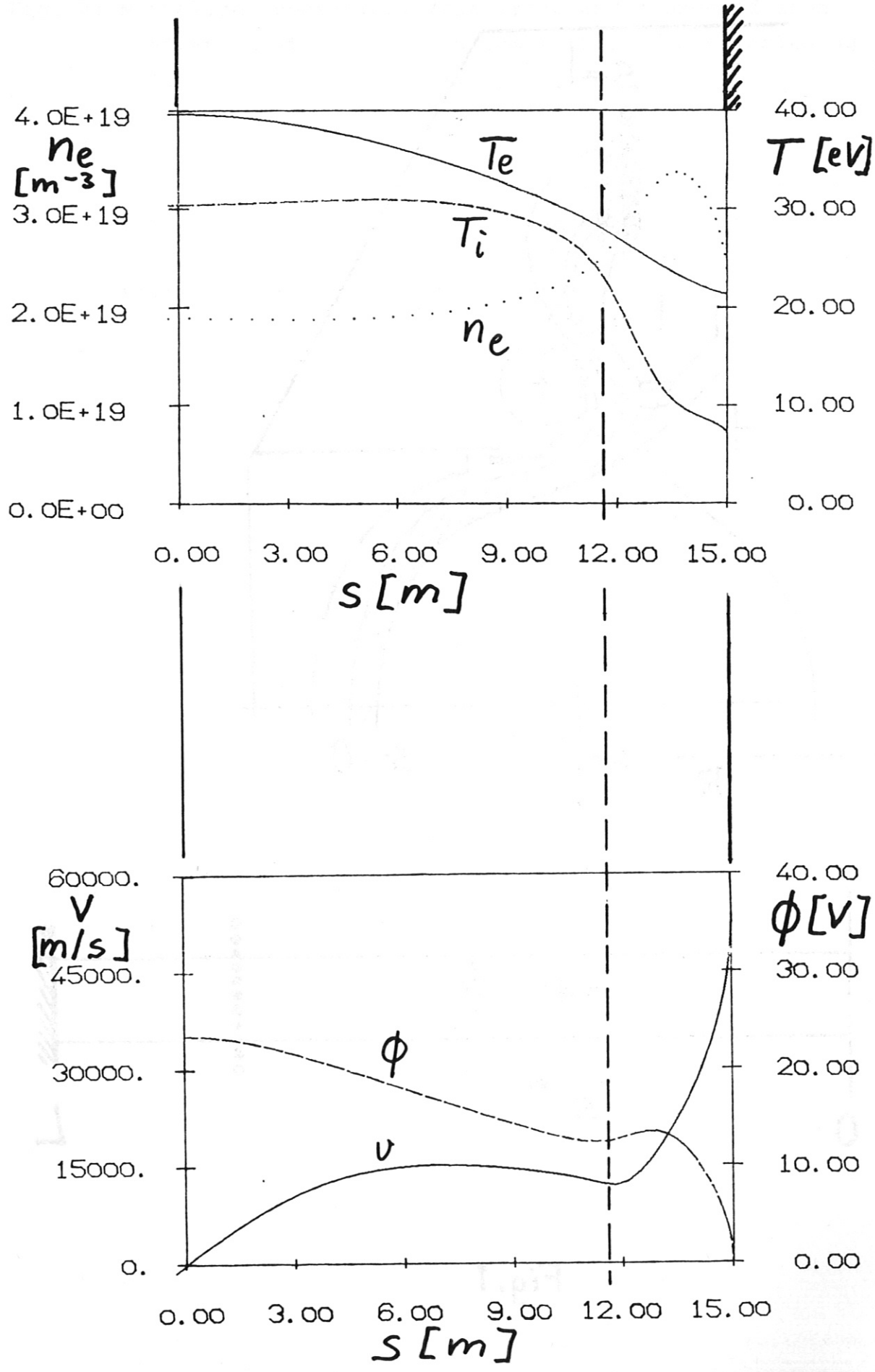
4.0E+19
n_e [m^{-3}]
3.0E+19
2.0E+19
1.0E+19
0.0E+00
40.00
T [eV]
30.00
20.00
10.00
0.00
T_e
T_i
n_e
0.00
3.00
6.00
9.00
12.00
15.00
s [m]
60000.
V [m/s]
45000.
30000.
15000.
0.
40.00
ϕ [V]
30.00
20.00
10.00
0.00
ϕ
v
0.00
3.00
6.00
9.00
12.00
15.00
s [m]

Fig. 3

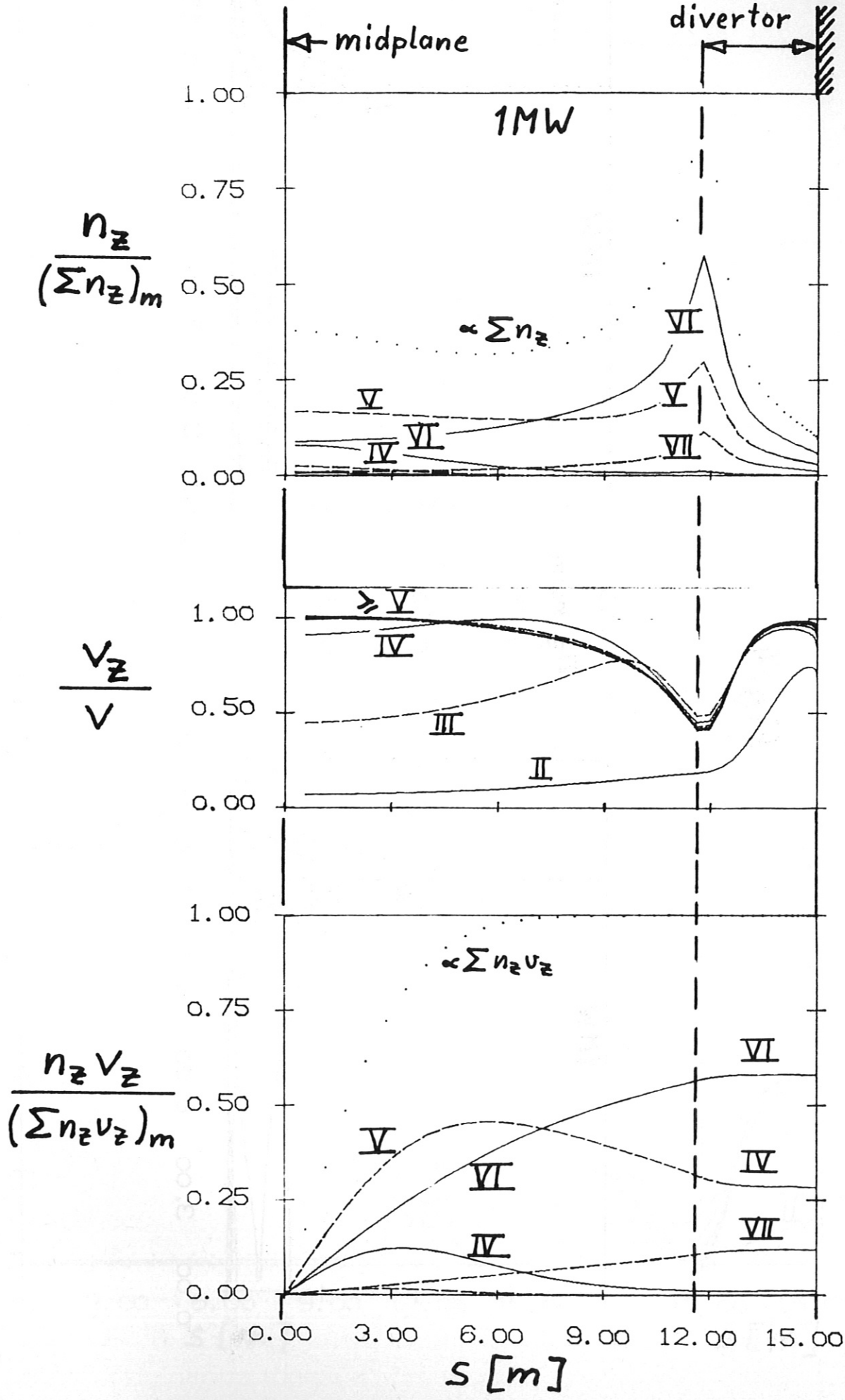
midplane
divertor
1MW
$\frac{n_z}{(\Sigma n_z)_m}$
$\propto \Sigma n_z$
$\frac{v_z}{v}$
$\propto \Sigma n_z v_z$
$\frac{n_z v_z}{(\Sigma n_z v_z)_m}$
1.00
0.75
0.50
0.25
0.00
0.00
3.00
6.00
9.00
12.00
15.00
s [m]

Fig. 4

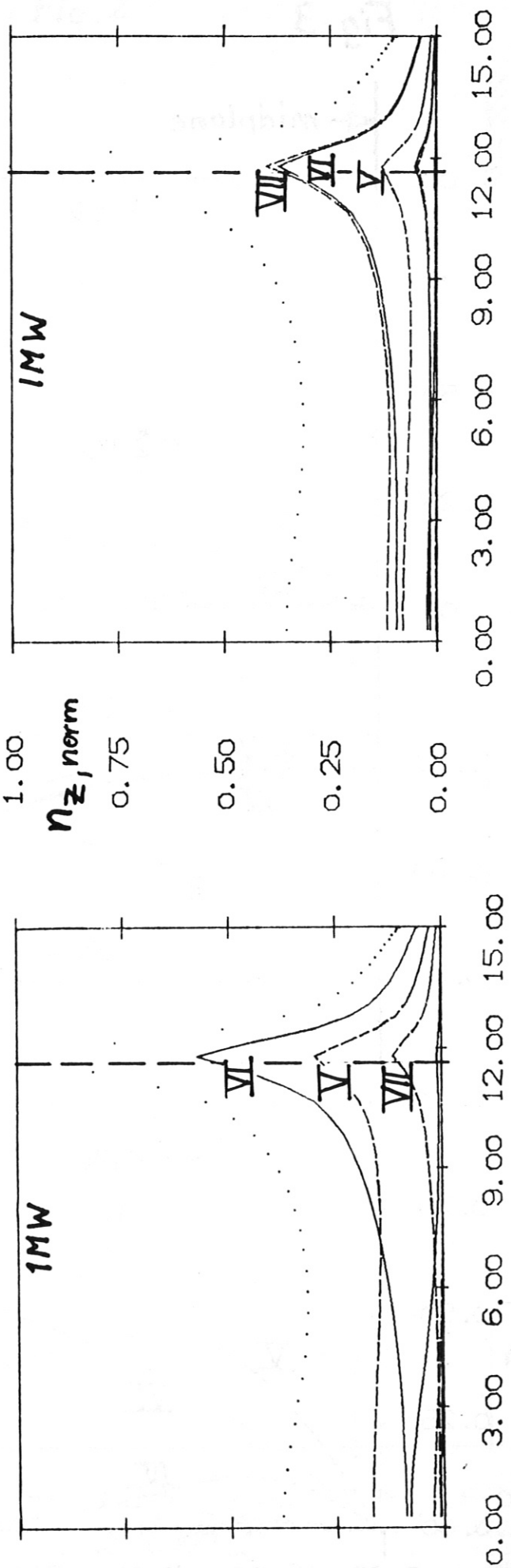
1MW
1MW
$\eta_{z,norm}$
1.00
0.75
0.50
0.25
0.00
0.00
3.00
6.00
9.00
12.00
15.00
VI
V
VII
VIII
II
V

Fig. 5

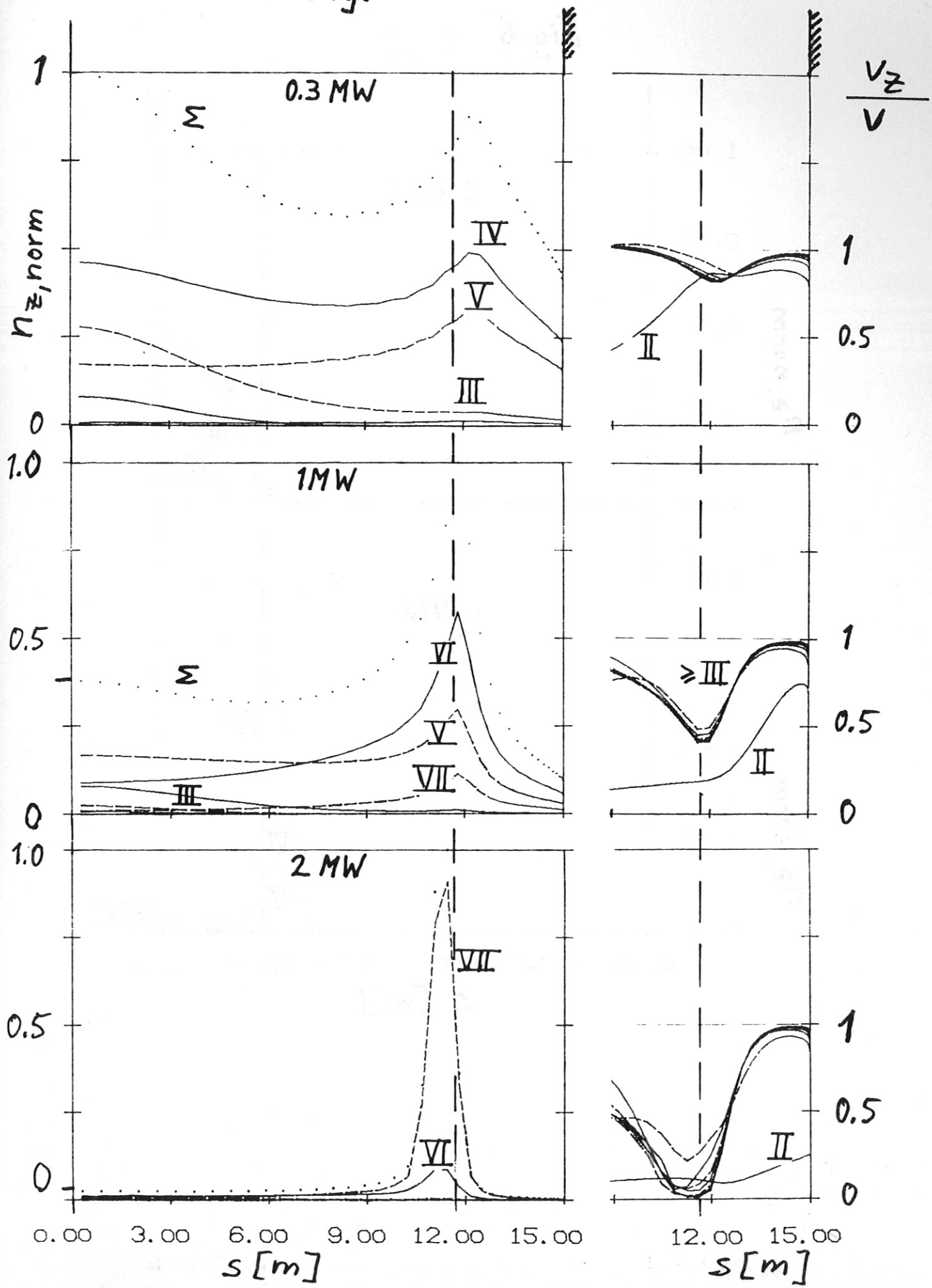
0.3 MW
Σ
IV
V
III
II
1MW
VI
VII
2 MW
$n_{z,norm}$
$\frac{v_z}{v}$
1
0.5
0
1.0
0.00
3.00
6.00
9.00
12.00
15.00
s [m]

Fig.6

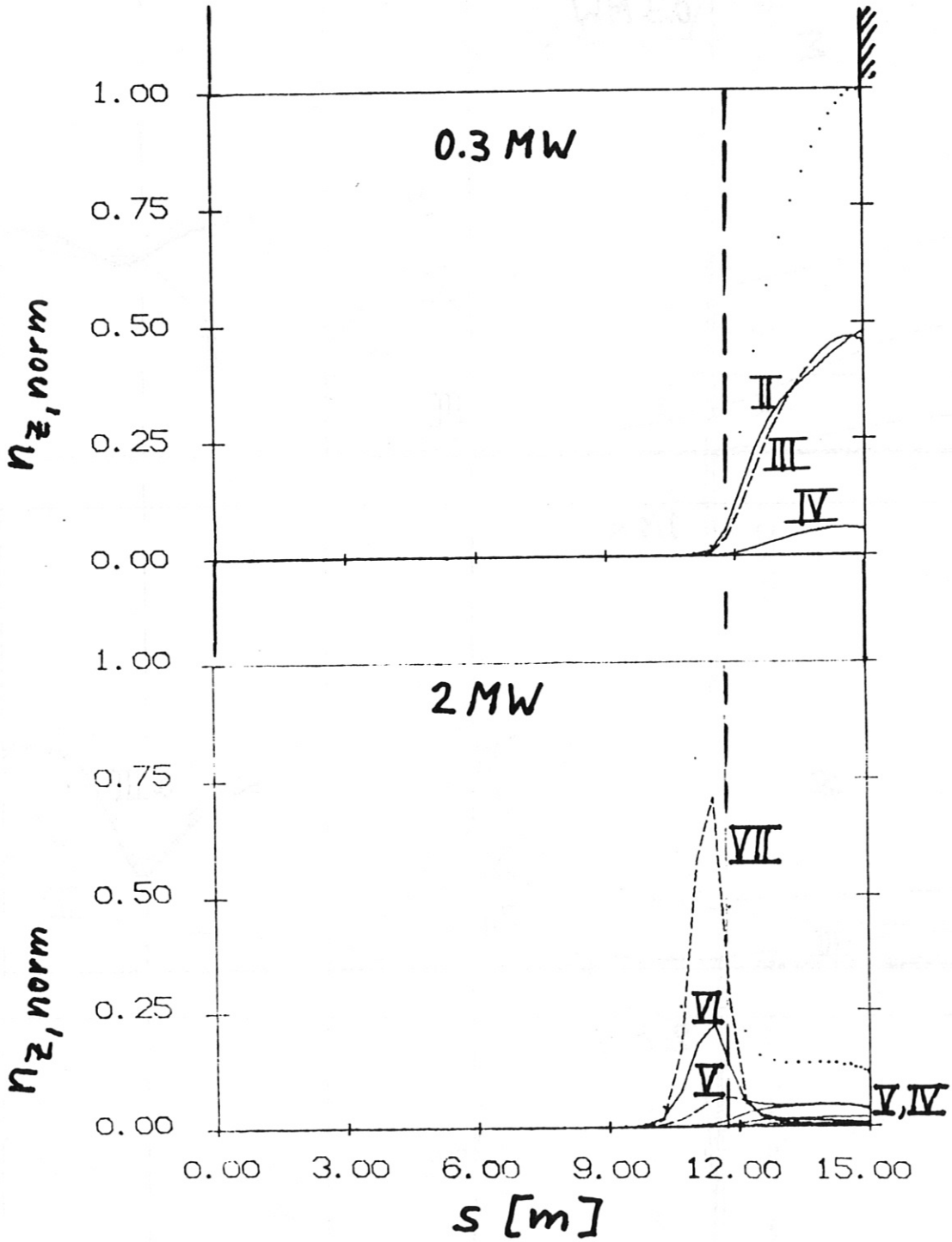
1.00
0.75
0.50
0.25
0.00
0.3 MW
II
III
IV
1.00
2 MW
0.75
0.50
0.25
0.00
VII
VI
V
V,IV
$\eta_{z,norm}$
$\eta_{z,norm}$
0.00
3.00
6.00
9.00
12.00
15.00
s [m]

Fig. 7

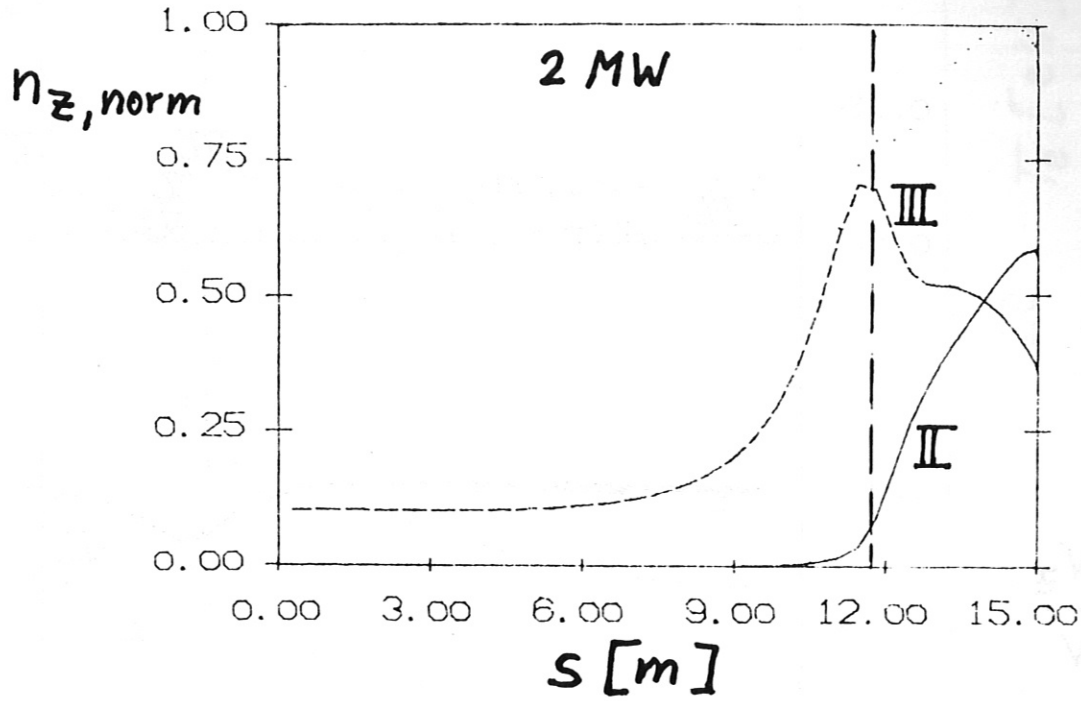
1.00
$n_{z,norm}$
2 MW
0.75
0.50
0.25
0.00
III
II
0.00
3.00
6.00
9.00
12.00
15.00
s [m]

Fig. 8

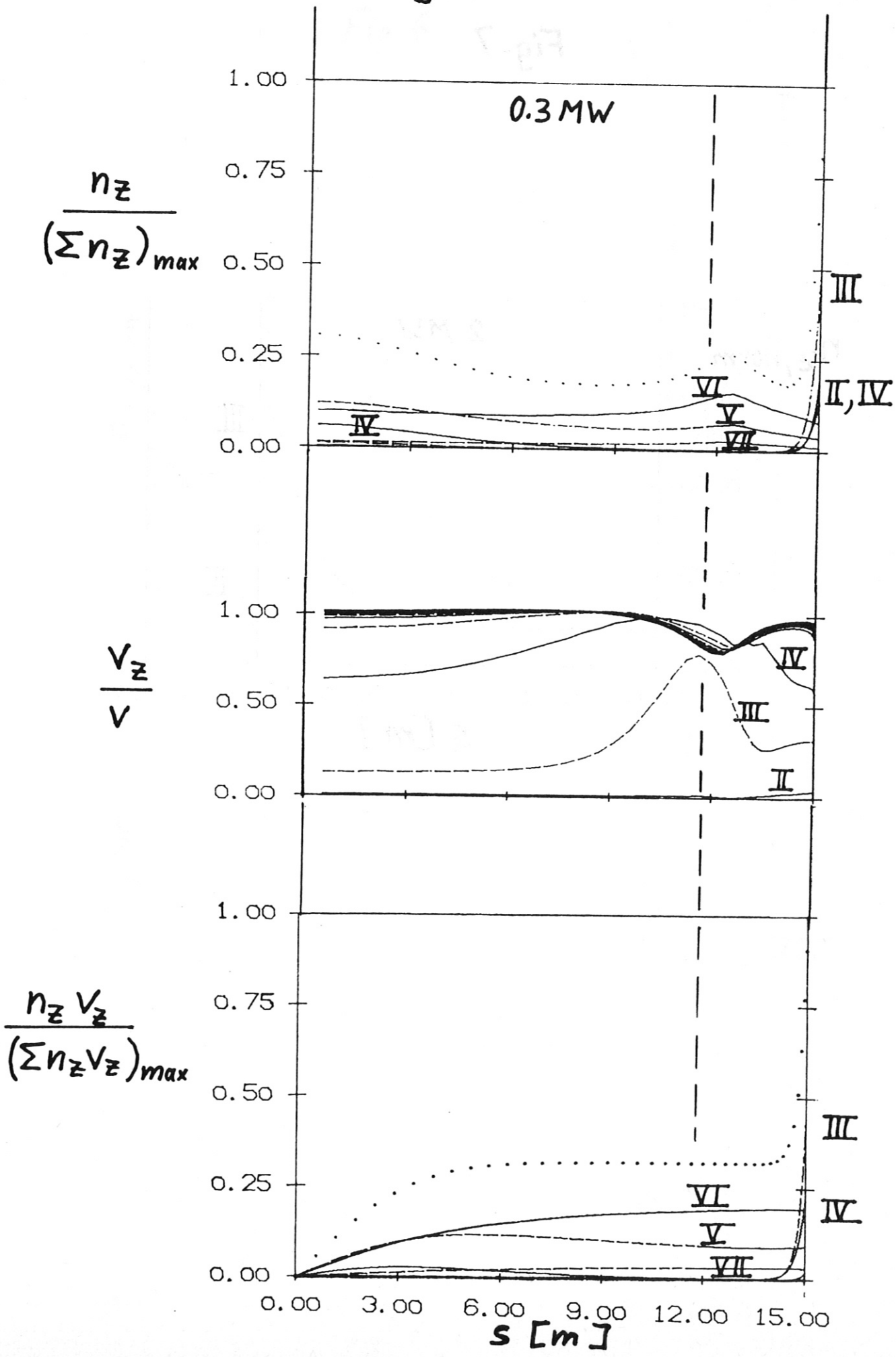
0.3 MW
$\frac{n_z}{(\Sigma n_z)_{max}}$
$\frac{V_z}{V}$
$\frac{n_z V_z}{(\Sigma n_z V_z)_{max}}$
1.00
0.75
0.50
0.25
0.00
III
II, IV
VI
V
IV
VII
IV
III
II
III
IV
VI
V
VII
0.00
3.00
6.00
9.00
12.00
15.00
s [m]

Fig. 9

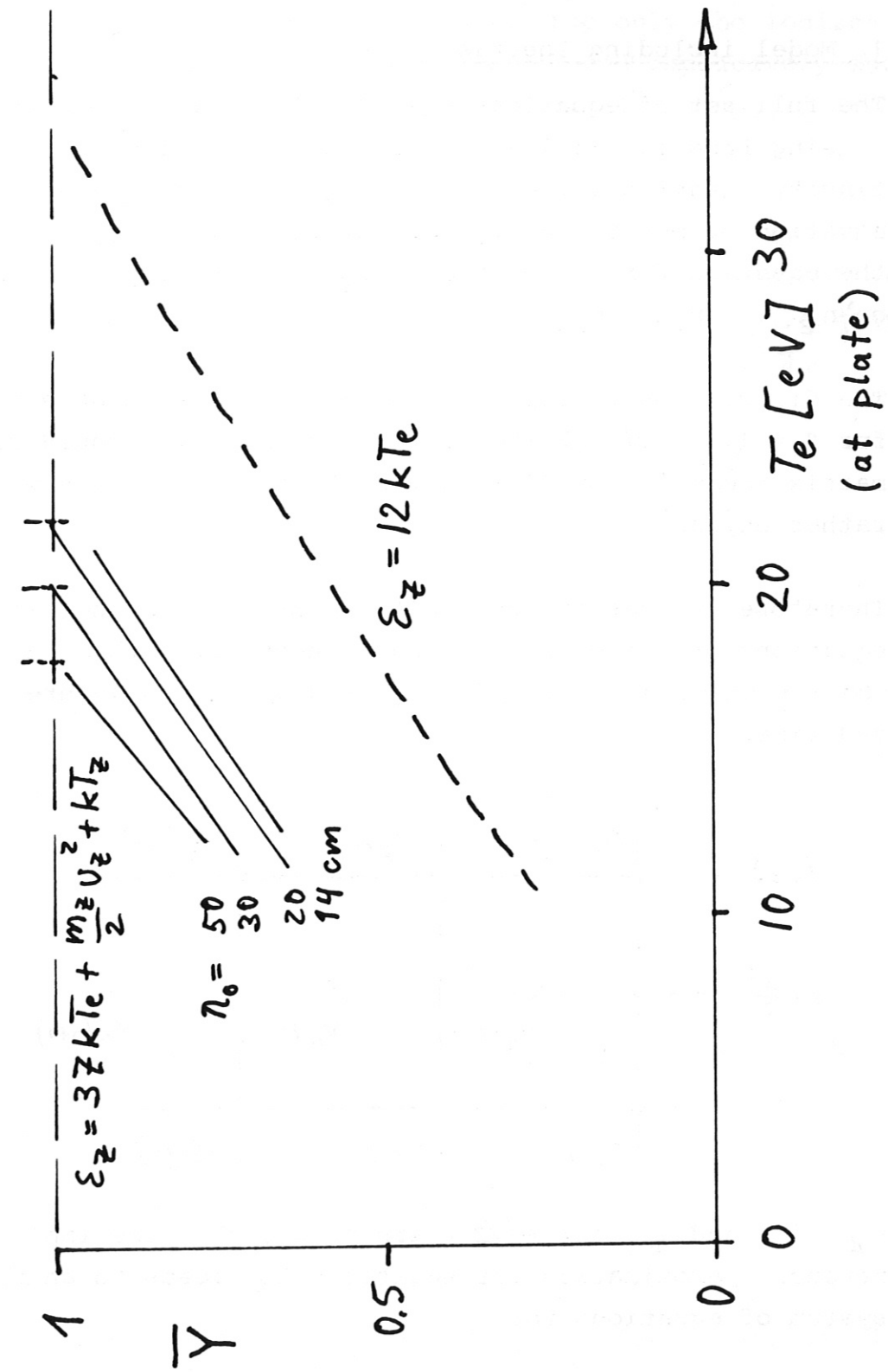
1
0.5
0
$\overline{Y}$
$\varepsilon_z = 3 z \overline{kT_e} + \overline{\frac{m_z}{2} v_z^2} + \overline{kT_z}$
n_o = 50
30
20
14 cm
$\varepsilon_z = 12\, kT_e$
0
10
20
30
T_e [eV]
(at plate)

Appendix A: Numerical Solution for Different Models

1. Model including Inertia

The full set of equations eqs. (1,3) contains coupling terms arising from ionization and recombination, i.e. in the continuity equation for n_z appear n_{z-1} and n_{z+1} and in the equation of motion for v_z appear v_{z-1} and v_{z+1}. Furthermore, the equation for n_z depends on v_z and the equation for v_z on n_{z-1} , n_z , n_{z+1} .

The direct simultanous solution of this system of equations for $Z = 1, \ldots N$ charge states for $\{n_z , v_z\}$ would require matrix inversion of (2 x N, 2 x N) matrices, which would be rather expensive.

Therefore the set of continuity equations and the set of the equations of motion are solved sequentially; this can be done consistently, if the grids for n_z and v_z are staggered in space and time.

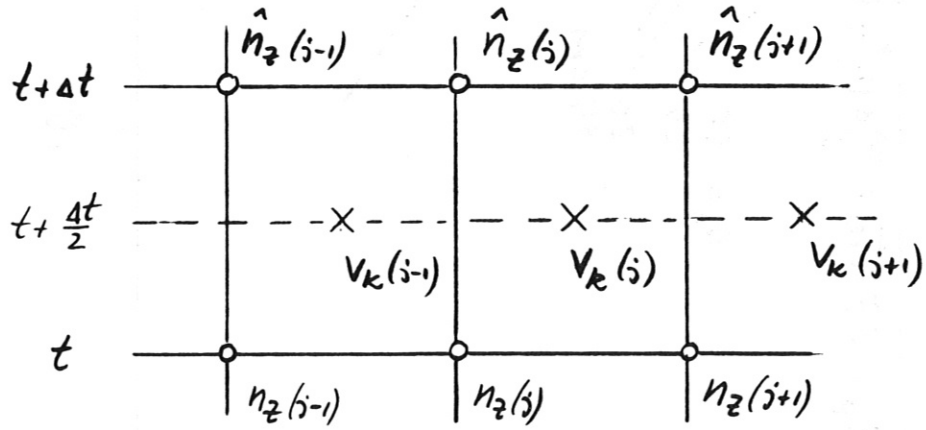

$n_{z,j}(t)$ and $v_{z,j}(t + \Delta t/2)$ are known; then the implicit difference approximation for equations n_z leads to an algebraic system of equations for

$$\hat{n}_{z;(j-1,j,j+1)}(t+\Delta t)$$

which only depends on $V_z(t+\frac{\Delta t}{2})$, which is known.

This set of equations for n_z , $z = 1, \ldots N$ is solved by the algorithm described in /19/; i.e. in one step only the ionization terms (containing $\hat{n}_{z-1}$, $\hat{n}_z$) are treated implicitely and in a second step only the recombination terms ($\hat{n}_z$, $\hat{n}_{z+1}$) are taken into account implicitly.

The solution for the equations of motion (i.e. advance $v_{z,s}(t + \frac{\Delta t}{2})$ to $\hat{v}_{z,s}$ $(t + \frac{\Delta t}{2} + \Delta t)$, where $\hat{n}_{z,s}$ $(t + \frac{\Delta}{2}t)$ is already known) is the carried out similarly. Hereby the nonlinear term $V_z \frac{\partial}{\partial s} V_z$ is properly linearized; an artificial visconsity term $\frac{\partial}{\partial s} q_z$ (Richtmyer-Morton)

$$q_z = \begin{cases} L^2 m_z n_z \left(\frac{\partial V_z}{\partial s}\right)^2 & \text{if} \quad \frac{\partial V_z}{\partial s} < 0 \\ 0 & \text{if} \quad \frac{\partial V_z}{\partial s} \geq 0 \end{cases}$$

is put into the equation to stabilize possible shock waves.

2. Without Inertia

If in the equations of motion (3) the inertia terms are omitted, one can express V_z algebraicly:

$$n_z V_z = -D^* \frac{\partial}{\partial s} n_z + n_z V_z^*$$

where

$$D^* = \frac{\tau_z}{m_z} k T_z$$

$$V_z^* = V - \frac{\tau_z}{m_z} \left\{ \frac{\partial}{\partial s} k T_z - ze E - \alpha_z \frac{\partial}{\partial z} k T_e - \beta_z \frac{\partial}{\partial s} k T_i \right\}$$

and substitute this into eq. (1); thus:

$$\frac{\partial}{\partial t} n_z - \frac{\partial}{\partial s}\left(D^* \frac{\partial}{\partial s} n_z\right) + \frac{\partial}{\partial s}\left(n_z V_z^*\right) =$$

$$= S_{z-1} n_{z-1} - (S_z + R_z) n_z + R_{z+1} n_{z+1} + \alpha_z$$

This set of equations for $\{n_z\}$ is then parabolic, since beside the drift-term $\frac{\partial}{\partial s}(n_z V_z^*)$ there appears a diffusion term. For this type of equation the algorithm /19/ was originally developed.

Appendix B: Results for Restricted Physical Models

In order to assess the importance of various physical effects, we present results for restricted physical model assumptions, i.e. we neglegt the corresponding terms in the equations of motion (equ. (3)).

The background plasma parameters are again those shown in fig. 2 and oxygen is the reference impurity. A Gaussian OII source at the midplane is assumed in exactly the same form as for the first oxygen example in the main text. Therefore, the results for restricted models presented below must be compared with those for the full model equations presented in fig. 3 of the main paper.

1. Inertia terms neglected

As a first example we drop the inertia terms, i.e. we replace equ. (3) by

$$\frac{\partial}{\partial s} P_z - n_z Z e E - g_z \frac{(v - v_z)}{\tau_z} - n_z \alpha_z \frac{\partial (k T_e)}{\partial s} - n_z \beta_z \frac{\partial (k T_i)}{\partial s} = 0$$

This set of equations allows for a simpler numerical solution as pointed out in appendix A. Fig. B-I shows the charge state densities and flow velocities. Compared to the full model (fig. 3), a significant change occurs only with respect to the velocity of low charge states. These are flowing now faster than the hydrogen background, since there is no retardation by inertia. The driving force for these states is mainly their individual pressure gradient with some contribution from the electric field. For high-Z the friction and thermal forces, both scaling as Z^2, are dominant.

While inertia seems to be less important in this case, there are also problems, where these terms must be definitely kept, e.g. for sources in the divertor chamber. An example is the iron self-sputtering case shown in fig. 8. Neglecting inertia, all charge states hit the target plate at a velocity, which is a few percent higher

than the hydrogen velocity. The resulting impact energy is about 500 eV in this case, causing a self-sputtering avalanche ($Y_z > 1$), where the full model yielded only an average self-sputtering coefficient of $\bar{Y} = 0.68$.

2. Thermal forces neglected

Now we keep the inertia terms but neglect the thermal forces ($\alpha_Z = \beta_Z = 0$ in equ. (3)). In addition, thermoelectric terms in the hydrogen background model, arising from thermal forces between hydrogen ions and electrons /11/, must be dropped in order to get a self-consistent description. The corresponding change of the background plasma, however, is rather small. A significant change occurs only for the electric field which now is approximately $E = -\partial p_e / \partial s$ (compare equ. (2)).

As expected, the impurity accumulation in front of the divertor recycling region disappears and the velocity is close to the background velocity everywhere, except for the lowest charge states (fig. B-II). Of course, the change is much more spectacular for the high recycling case shown in fig. 5c, which, without thermal forces, behaves also quite similar to fig. B-II. Therefore, a calculation ignoring thermal forces would be completely misleading for these cases.

3. No slip motion between hydrogen and impurities

As an extreme simplification we may neglect any slip between hydrogen and impurities. Equation (3) is then simply replaced by

$$v_z = v$$

and we ask only for the charge state distribution at prescribed flow velocity. Fig. B-III shows that there is little difference with respect to the density distribution compared to fig. B-II. The reason is that without thermal forces the flow velocity of the most prominent charge states was already close to the background velocitiy. Therefore, this simple model is definitely restricted to cases where thermal forces are negligible ($M \gg n_i / n_T$) and where the collisional drag is the dominant effect also compared to the other contributions in equ. (3).

Fig. B-I

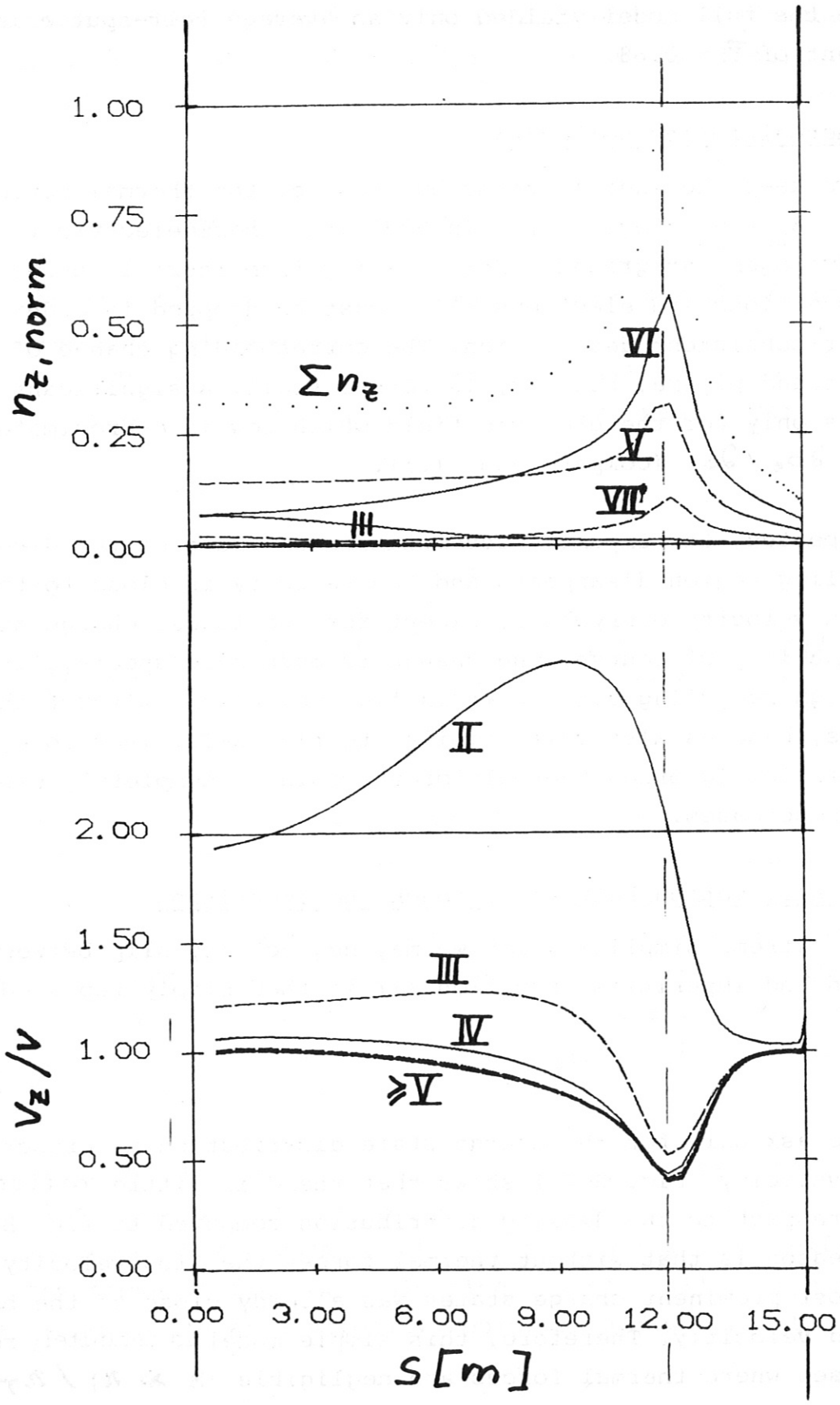
1.00
0.75
0.50
0.25
0.00
$n_{z,norm}$
Σn_z
VI
V
VII
III
II
2.00
1.50
1.00
0.50
0.00
v_z/v
III
IV
V
0.00
3.00
6.00
9.00
12.00
15.00
s[m]

Fig. B-II

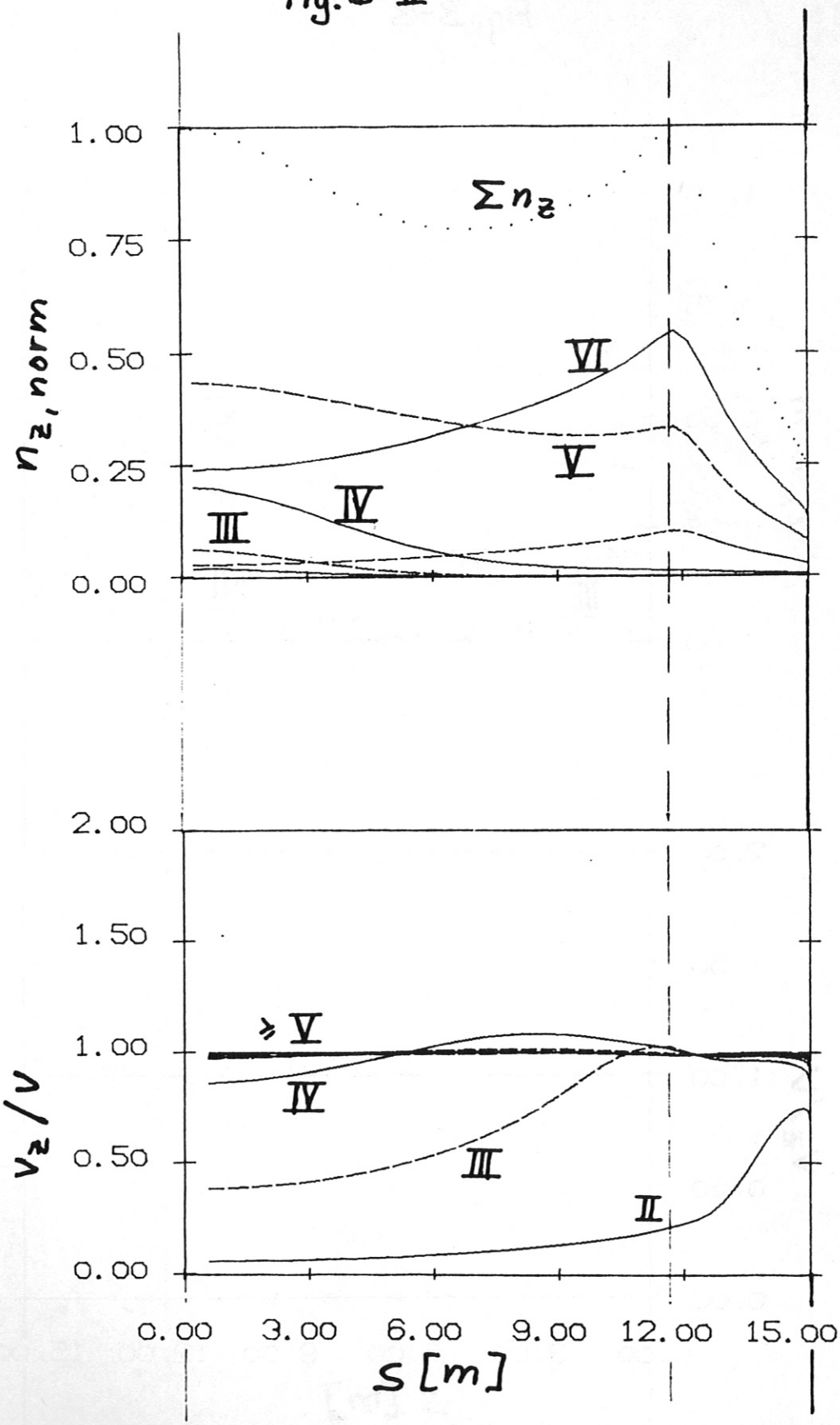
1.00
0.75
0.50
0.25
0.00
$n_{z,norm}$
Σn_z
VI
V
IV
III
2.00
1.50
1.00
0.50
0.00
v_z / v
≈ V
IV
III
II
0.00
3.00
6.00
9.00
12.00
15.00
s [m]

Fig. B-3

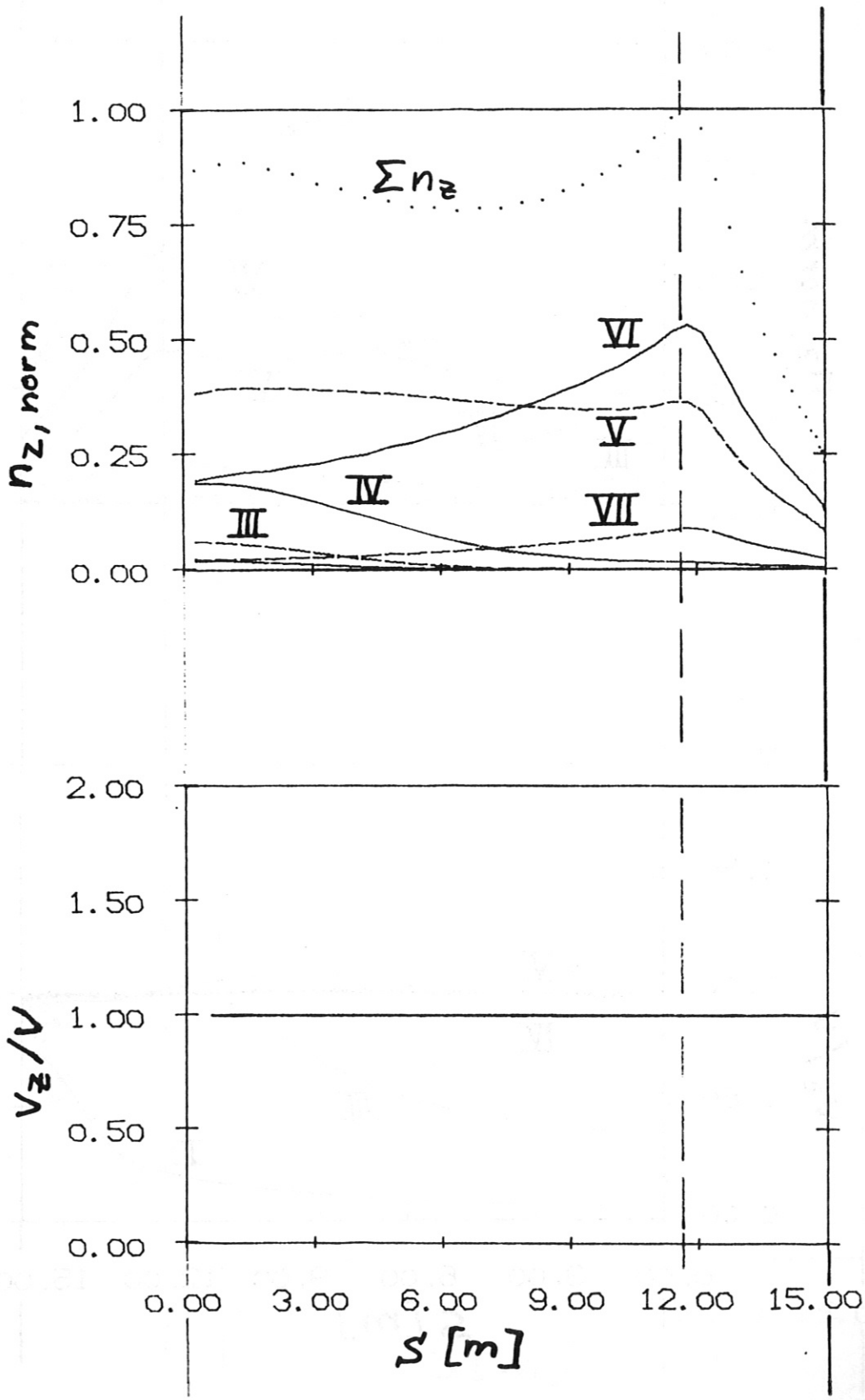
1.00
0.75
0.50
0.25
0.00
Σn_z
VI
V
IV
III
VII
$n_{z,norm}$
2.00
1.50
1.00
0.50
0.00
v_z/v
0.00
3.00
6.00
9.00
12.00
15.00
s [m]